

Article

Selective Separation of Rare Earth Ions from Mine Wastewater Using Synthetic Hematite Nanoparticles from Natural Pyrite

Chunxiao Zhao ^{1,2}, Jun Wang ^{1,2,*}, Baojun Yang ^{1,2}, Yang Liu ^{1,2,*} and Guanzhou Qiu ^{1,2}

¹ School of Minerals Processing & Bioengineering, Central South University, Changsha 410083, China; zhaocx@csu.edu.cn (C.Z.); 22021048@csu.edu.cn (B.Y.); gqz@csu.edu.cn (G.Q.)

² Key Lab of Biohydrometallurgy of Ministry of Education, Changsha 410083, China

* Correspondence: wjwq2000@126.com (J.W.); liuyang2022@csu.edu.cn (Y.L.)

Abstract: The separation of rare earth ions (RE³⁺) from aqueous solutions poses a significant challenge due to their similar chemical and physical characteristics. This study presents a method for synthesizing hematite nanoparticles (Fe₂O₃ NPs) through the high-temperature phase transition of natural pyrite for adsorbing RE³⁺ from mine wastewater. The characteristics of Fe₂O₃ NPs were studied using XRD, SEM, BET, XPS, FTIR, and Zeta potential. The optimal condition for RE³⁺ adsorption by Fe₂O₃ NPs was determined to be at pH 6.0 with an adsorption time of 60 min. The maximum adsorption capacities of Fe₂O₃ NPs for La³⁺, Ce³⁺, Pr³⁺, Nd³⁺, Sm³⁺, Gd³⁺, Dy³⁺, and Y³⁺ were 12.80, 14.02, 14.67, 15.52, 17.66, 19.16, 19.94, and 11.82 mg·g⁻¹, respectively. The experimental data fitted well with the Langmuir isotherm and pseudo-second-order models, suggesting that the adsorption process was dominated by monolayer chemisorption. Thermodynamic analysis revealed the endothermic nature of the adsorption process. At room temperature, the adsorption of RE³⁺ in most cases (La³⁺, Ce³⁺, Pr³⁺, Nd³⁺, Sm³⁺, and Y³⁺) onto Fe₂O₃ NPs was non-spontaneous, except for the adsorption of Gd³⁺ and Dy³⁺, which was spontaneous. The higher separation selectivity of Fe₂O₃ NPs for Gd³⁺ and Dy³⁺ was confirmed by the separation factor. Moreover, Fe₂O₃ NPs exhibited excellent stability, with an RE³⁺ removal efficiency exceeding 94.70% after five adsorption–desorption cycles, demonstrating its potential for the recovery of RE³⁺ from mine wastewater.



Citation: Zhao, C.; Wang, J.; Yang, B.; Liu, Y.; Qiu, G. Selective Separation of Rare Earth Ions from Mine Wastewater Using Synthetic Hematite Nanoparticles from Natural Pyrite. *Minerals* **2024**, *14*, 464. <https://doi.org/10.3390/min14050464>

Academic Editor: Ismail Md. Mofizur Rahman

Received: 27 March 2024

Revised: 12 April 2024

Accepted: 24 April 2024

Published: 28 April 2024



Copyright: © 2024 by the authors. Licensee MDPI, Basel, Switzerland. This article is an open access article distributed under the terms and conditions of the Creative Commons Attribution (CC BY) license (<https://creativecommons.org/licenses/by/4.0/>).

Keywords: rare earth elements; hematite nanoparticles; pyrite; adsorption; separation selectivity

1. Introduction

Rare earth elements (REEs) play a crucial role in advancing modern technology and have widespread applications in environmental protection, energy production, digital technology, and medical applications [1]. However, the traditional extraction process of REEs leads to a loss of approximately 10% in yield, resulting in over 20 million tons of wastewater annually with REEs concentrations ranging from 1 to 100 mg·L⁻¹ [2,3]. With the growing demand for REEs and their compounds, the recycling of REEs from mine wastewater has received considerable attention [4]. Additionally, similar to other heavy metals, REEs can be accumulated in ecosystems, posing potential risks to the environment and human health [5,6]. Studies have shown that REEs can cause liver and lung cytotoxicity, damage the reproductive system, and lead to neural tube defects [7,8]. Therefore, the recovery of REEs from mine wastewater is becoming an increasingly promising option [9].

To date, various methods including ion exchange, chemical precipitation, solvent extraction, and adsorption have been developed for the separation and recovery of REEs [6]. Each method has its advantages and disadvantages. For example, ion exchange is known for its simple operation and effective separation but lacks continuous processing capability and is time-consuming [10]. The chemical precipitation method is cost-effective and easy to operate but is primarily suitable for high-concentration REEs separation [11]. Solvent extraction offers low energy consumption and wide applicability but poses environmental pollution problems due to the use of organic solvents [12]. While new

unconventional processes have recently been developed by Faur et al. and Xu et al., they are not yet industrialized for reasons of optimization [13–15]. Among these methods, adsorption stands out as a practical, efficient, environmentally friendly, and cost-effective approach for treating wastewater with low REE concentrations [16]. Numerous adsorbents such as O-modified coordination polymer [11], Ca-alginate/carboxymethyl chitosan/ $\text{Ni}_{0.2}\text{Zn}_{0.2}\text{Fe}_{2.6}\text{O}_4$ magnetic bionanocomposite [16], magnetic $\text{Fe}_3\text{O}_4/\text{MnO}_2$ decorated reduced graphene oxide [9], functionalized magnetite nanoparticles [17], and magnetic mesoporous $\text{Fe}_3\text{O}_4@\text{mSiO}_2$ -DODGA nanoparticles [12] have been developed for the adsorption of REEs. Magnetic nanoparticles in particular have received interest for their excellent separation and regeneration capabilities [17]. However, researchers still encounter the challenge of devising simple and cost-effective methods for preparing magnetic nanoparticle adsorbents with desirable adsorption properties.

Natural pyrite is abundant, inexpensive [18], and considered as an industrial solid waste [19]. Furthermore, rare earth minerals and pyrite sometimes coexist. For instance, the conglomerate beds of rare earth minerals in Eco Ridge Mine contain 5% to 15% pyrite [20]. Studies have demonstrated that pyrite can be transformed into hematite magnetic nanoparticles through the high-temperature phase transition [21], which occurs without the use of chemical reagents. Hematite has been proven to be an effective and environmentally friendly adsorbent for removing inorganic heavy metal ions such as Cr^{4+} , As^{3+} , As^{5+} , UO_2^{2+} , Pb^{2+} , and Cu^{2+} [22–25]. In particular, rare earth ions (RE^{3+}) have an affinity for adsorption with iron oxides according to previous studies [20,26]. However, the potential of hematite converted from natural pyrite to adsorb RE^{3+} remains unexplored.

Therefore, in this paper, hematite nanoparticles (Fe_2O_3 NPs) were synthesized by the high-temperature phase transition of pyrite for the recovery of mixed RE^{3+} from mine wastewater. The synthesized product was characterized using scanning electron microscopy (SEM), X-ray diffraction (XRD), Brunauer–Emmett–Teller (BET), Fourier-transform infrared spectroscopy (FTIR), and Zeta potential. The effect of time, pH, initial RE^{3+} concentration, and temperature on the adsorption efficiency of RE^{3+} was investigated through batch adsorption experiments. Furthermore, the experimental data were fitted with classical kinetic and isotherm models, and the thermodynamic parameters (ΔS° , ΔG° , and ΔH°) were evaluated to provide insights into the adsorption process. The proposed method of utilizing Fe_2O_3 NPs derived from pyrite as an adsorbent for RE^{3+} provides a cost-effective and efficient solution for the recovery of RE^{3+} in aqueous solutions while also increasing the utilization value of pyrite.

2. Material and Methods

2.1. Materials and Reagents

The RE^{3+} solution used for the adsorption experiments was prepared by diluting a standard RE^{3+} solution ($100 \text{ mg}\cdot\text{L}^{-1}$) [27]. The pH of the solution was adjusted using either 0.1 M sodium hydroxide or nitric acid solution and monitored with a pH meter [28]. Anhydrous ethanol was obtained from Sinopharm Chemical Reagent Co., Ltd., Shanghai, China. All chemicals and reagents were of analytical grade and used as received. The mine wastewater used in this study was collected from an ion adsorption rare earth mine in Hunan, China. The concentration of the main metal ions in the wastewater was determined by inductively coupled plasma mass spectrometry (ICP-MS) after filtration through a $0.22 \mu\text{m}$ filter membrane [29], and the results are presented in Table 1. Pyrite samples were taken from Hubei, China, ground using a vibratory mill, and sieved to ensure that the particle size was between $38 \mu\text{m}$ and $74 \mu\text{m}$ for subsequent studies. The selected pyrite was found to be of high purity based on XRD analysis (Figure S1).

Table 1. Concentrations of various ions in the mine wastewater used in this study.

Ions	Concentration (mg·L ⁻¹)
Y	3.019
La	1.630
Nd	1.461
Dy	0.432
Gd	0.399
Pr	0.356
Sm	0.341
Ce	0.327
Ca	34.884
K	11.151
Na	7.502
Mg	5.982
Al	3.060
Mn	2.025

2.2. Preparation of Fe₂O₃ NPs

The pyrite was further ground using a planetary ball mill (YXQM-4L, MITR) [30]. In the grinding process, an orthogonal experiment L₉(3⁴) was designed by specifying ball-to-material ratios (10:1, 15:1, and 20:1), rotation speeds (400, 500, and 600 rpm), and grinding times (1, 2, and 3 h) as factors A, B, and C, respectively. Experimental details are presented in Tables S1 and S2. Subsequently, the finely ground pyrite was subjected to high-temperature calcination in a muffle furnace at various temperatures and durations to convert it into hematite [21]. The heating and cooling rates were both 10 °C·min⁻¹, and the sample was taken out after dropping to room temperature. Finally, Fe₂O₃ NPs were obtained by grinding the calcined product in an agate mortar using anhydrous ethanol as a dispersant [23].

2.3. Adsorption and Desorption Experiments

The adsorption capacity of Fe₂O₃ NPs to mixed RE³⁺ in solution was investigated by batch adsorption experiments. The experiments were conducted in 250 mL Erlenmeyer flasks placed on a magnetic stirrer at room temperature. The initial concentration of RE³⁺ was 5 mg·L⁻¹ each, with 50 mg of Fe₂O₃ NPs, a pH of 5.0, and a solution volume of 50 mL. Various adsorption times (2–240 min) were tested to determine the time required for adsorption equilibrium and for kinetic analyses. The optimal pH for adsorption was determined by testing different initial pH values ranging from 2.0 to 7.0 [31]. Additionally, thermodynamic adsorption experiments were conducted at three different temperatures (298, 308, and 318 K). Isothermal adsorption experiments were performed at initial RE³⁺ concentrations of 5–40 mg·L⁻¹. All experiments were performed in triplicate. Kinetic and isothermal models were fitted using the Origin software (version 2021), optimizing the model parameters to minimize the difference between the predicted and observed values. After reaching adsorption equilibrium, the concentration of RE³⁺ in the solution was measured by ICP-MS after filtration with a 0.22 µm filter membrane. The adsorption efficiency and capacity of RE³⁺ adsorbed on Fe₂O₃ NPs were calculated according to Equations (1) and (2) [32].

$$\text{Adsorption efficiency}(\%) = \frac{C_0 - C_e}{C_0} \times 100\% \quad (1)$$

$$q_t = \frac{(C_0 - C_t)V}{m} \quad (2)$$

where q_t (mg·g⁻¹) represents the adsorption capacity at time t ; C_0 (mg·L⁻¹), C_e (mg·L⁻¹), and C_t (mg·L⁻¹) denote the initial, equilibrium, and momentary concentrations of RE³⁺, respectively; V (L) refers to the solution volume; and m (g) is the adsorbent mass.

The recycling and regeneration experiments of Fe₂O₃ NPs were carried out as follows: a 50 mL solution containing 5 mg·L⁻¹ of RE³⁺ was mixed with 100 mg of Fe₂O₃ NPs for 1 h in each cycle. The mixed solution was then filtered using a 0.22 μm membrane, and the residual concentration of RE³⁺ was analyzed by ICP-MS. Desorption regeneration was achieved by agitating with 0.2 M HNO₃ for 1 h, followed by washing with pure water [16]. The cleaned and regenerated Fe₂O₃ NPs were then reintroduced into a fresh mixed RE³⁺ solution with the same concentration and volume, allowing for adsorption for 1 h. This process was repeated five times. Finally, the effectiveness of the Fe₂O₃ NPs for practical applications was evaluated by mixing 200 mg of the adsorbent with 50 mL of actual mine wastewater.

2.4. Characterizations

The particle size analysis of ground pyrite was performed with a laser particle size analyzer (MASTERSIZER 2000) (Malvern, Worcestershire, UK) [33]. Thermal behavior analysis was conducted using a thermal gravimetric analyzer (TGADTA, STA 449C/4/MFC/G/Jupiter[®], Bavaria, Germany) with a gas flow rate of 100 mL·min⁻¹ in an air atmosphere [34]. XRD analysis at 4–80° was used to determine the physical phase of pyrite after heat treatment [28]. The specific surface area and pore size distribution of the adsorbent were measured at 77 K using a specific surface area analyzer (Autosorb iQ) (Anton Paar, Graz, Austria) at a relative pressure of 0–1.0 [9]. Morphology and surface element composition were characterized with a scanning electron microscope (SEM; Nova NanoSEM 230, FEI Company, Hillsboro, OR, USA) equipped with an X-ray energy dispersive spectroscopy system (EDS). Nanoparticle size was analyzed by transmission electron microscopy (TEM, Talos F200i) (Thermo Fisher Scientific, Waltham, MA, USA). FTIR spectra were recorded using an FT-IR spectrometer (iS50, Thermo Fisher Scientific, Waltham, MA, USA) in the range of 4000–400 cm⁻¹ [35]. Elemental composition on the sample surface was determined by X-ray photoelectron spectroscopy (ESCALAB250) (Thermo Fisher Scientific, Waltham, MA, USA), with an analysis of the oxidation state of oxygen [28]. Zeta potential was measured using a Zeta point position analyzer (Nano ZS, Malvern Panalytical, Worcestershire, UK).

3. Results and Discussion

3.1. Preparation and Characterization of Fe₂O₃ NPs

For larger particles, the pyrolysis of pyrite is inhibited or shifted to higher temperatures due to slow gas diffusion [36]. As a result, the pyrite was crushed using a planetary ball mill. To investigate the impact of the ball-to-material ratio, rotation speed, and grinding time on the grinding process of pyrite, the particle size distribution and median size (D50) of the milled pyrite were analyzed [33]. D50 is a crucial parameter for measuring the size distribution, representing the point where half of the particle diameter is less than or equal to this value. A smaller D50 value indicates a finer particle distribution, while a larger D50 value suggests a coarser distribution [37]. The histograms of the particle size distribution and the cumulative distribution curves of the milled pyrite are presented in Figure 1. The analysis revealed a segment with a steep slope in the cumulative distribution curve, while the other segments appeared as nearly horizontal straight lines. This indicated significant fluctuations in the number of particles in the sloped segment, whereas there were almost no particles in the horizontal straight segment. The results of the orthogonal experiment demonstrated that the ball-to-material ratio had the most significant influence, with the rotation speed and grinding time showing a relatively lower degree of influence on the grinding particle size (Table 2). Based on the D50 results, A2B3C1 (ball-to-material ratio of 15:1, rotation speed of 600 rpm, and grinding time of 1 h) was selected for grinding to obtain finely ground pyrite samples suitable for calcination.

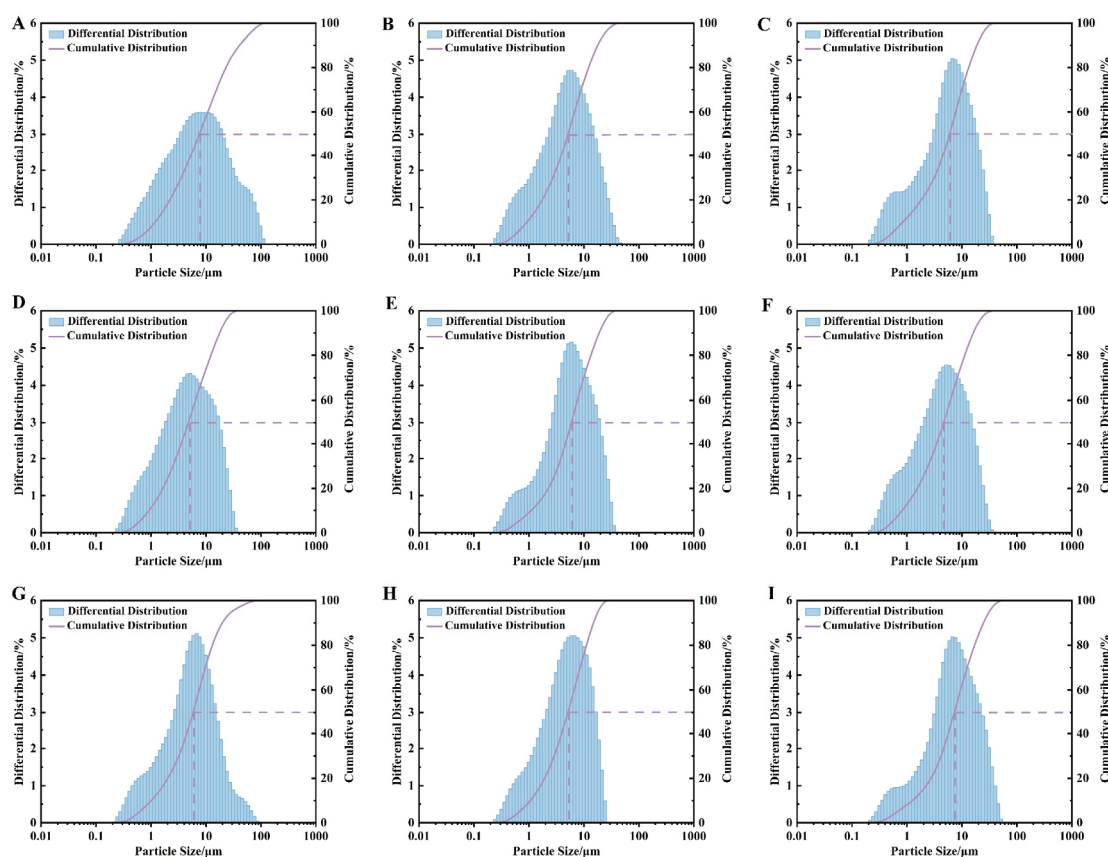


Figure 1. Particle size distribution histograms and cumulative distribution curves for milled pyrite ((A–I) represent the tests 1–9 of the orthogonal experiments of the grinding process of pyrite (Table S2)).

Table 2. Results of the orthogonal design experiments for pyrite ground by a planetary ball mill.

Test	Ball-to-Material Ratio (A)	Rotation Speed, Rpm (B)	Grinding Time, h (C)	D50 of Pyrite, μm
1	10:1	400	1	7.563
2	10:1	500	2	5.132
3	10:1	600	3	5.956
4	15:1	400	2	4.803
5	15:1	500	3	5.912
6	15:1	600	1	4.669
7	20:1	400	3	5.841
8	20:1	500	1	5.137
9	20:1	600	2	7.282
I	18.651	18.207	17.369	
II	15.384	16.181	17.217	
III	18.260	17.907	17.709	
K ₁	6.217	6.069	5.790	T = 52.295
K ₂	5.128	5.394	5.739	
K ₃	6.087	5.969	5.903	
R	1.089	0.675	0.164	

Notes: I, II, and III are the estimated values of the horizontal effects of 1, 2, and 3 on each corresponding column (factor), which are calculated as I_i (II_i , III_i) = sum of data corresponding to level 1 (2, 3) in column i ; K_i is the combined average of the data of level i = i /number of repetitions of level i ; the R line is called the extreme difference (maximum–minimum), indicating the magnitude of the effect of the factor on the results.

Figure 2A illustrates the TG-DTG-DSC curves of fine-grained pyrite from room temperature to 1000 °C in an air atmosphere. The results indicated that a reaction occurred

at 386.4 °C, leading to an increase in mass as pyrite transformed into sulfate (FeSO₄, Fe₂(SO₄)₃) [38], which further decomposed into iron oxide (Fe₂O₃) and sulfur dioxide (SO₂) [39]. Oxidation occurred at 493.8 °C, converting iron-containing substances into hematite (Fe₂O₃) at 699.9 °C [36]. Consequently, the thermal decomposition of fine-grained pyrite began at 386.4 °C and ended at 699.9 °C.

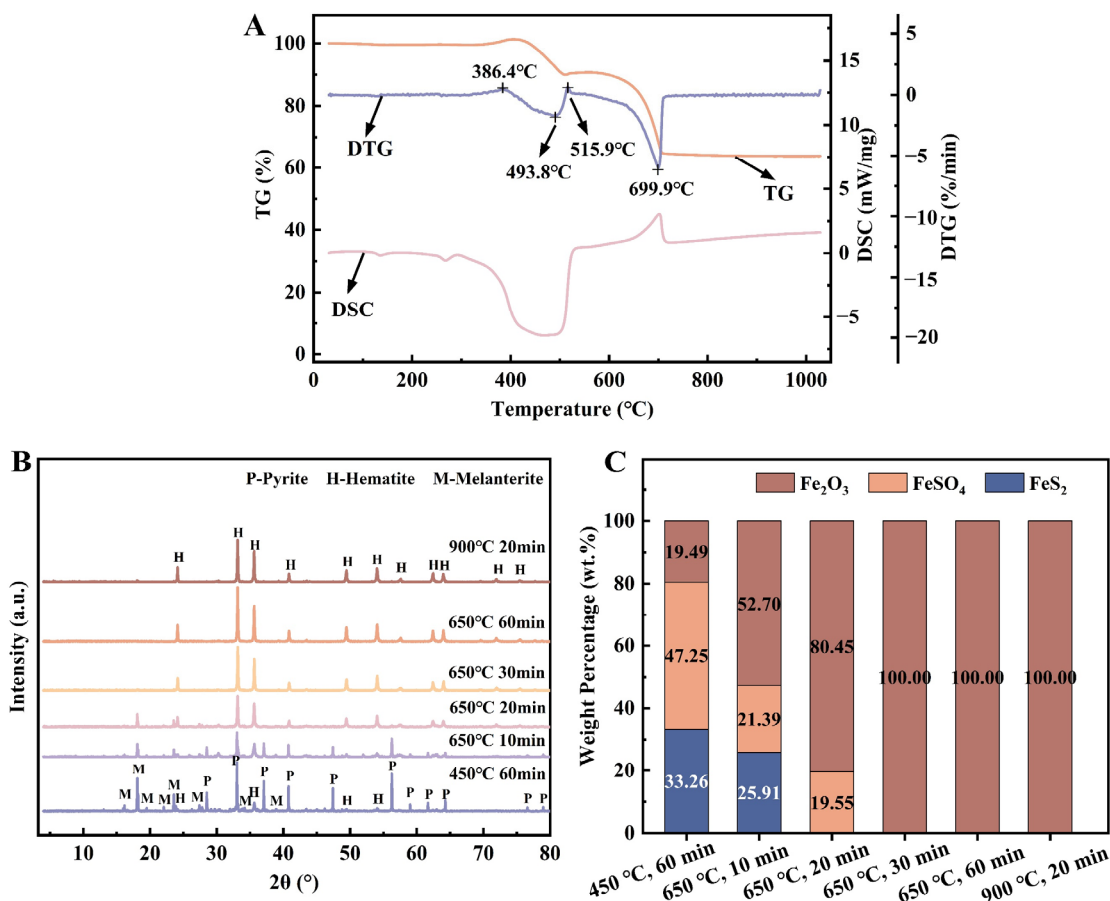


Figure 2. (A) TG-DTG-DSC curves for pyrite in the air atmosphere, (B) XRD patterns and (C) semi-quantitation analysis of pyrite after being calcined in the air atmosphere at different temperatures and times.

Various temperatures and calcination times were chosen to observe the phase transition of pyrite thermal decomposition, as depicted in Figure 2B,C. The results indicated that after being calcined at 450 °C for 60 min and at 650 °C for 10 min, some pyrite could still be detected. Additionally, FeSO₄ and hematite were detected. When the calcination conditions were set at 650 °C for 20 min, the pyrite completely disappeared, and the physical phase consisted solely of hematite and FeSO₄. When the calcination conditions were 650 °C for 30 min, 650 °C for 60 min, and 900 °C for 20 min, the pyrite phase was completely transformed into hematite. These findings were consistent with the results obtained from the thermogravimetric analysis. Thus, for economic reasons, the optimal calcination conditions were determined to be 650 °C for 30 min. Finally, the calcined products were ground with ethanol as a dispersant to prevent agglomeration [40] in the agate mortar [23]. The overall preparation scheme is illustrated in Figure 3.



Figure 3. Schematic illustration of the preparation of Fe_2O_3 NPs.

Figure 4 depicts the characteristics of fine-grained pyrite and Fe_2O_3 NPs. It was observed that the particle size of the sample significantly decreased after calcination (Figure 4A,B). The Fe_2O_3 NPs exhibited fine particles with a rough surface, ranging from 10 to 200 nm in size (Figure 4C,D), confirming the successful preparation of Fe_2O_3 NPs. Furthermore, the atomic ratio of Fe to O was approximately 2:3 (Figure 4E), indicating the complete conversion of pyrite to hematite, which aligned with the XRD results. The specific surface area, total pore volume, and average pore diameter of the Fe_2O_3 NPs were analyzed using the N_2 adsorption–desorption isotherm to be $14.12 \text{ m}^2 \cdot \text{g}^{-1}$, $0.061 \text{ cm}^3 \cdot \text{g}^{-1}$, and 17.36 nm, respectively (Figure 4F).

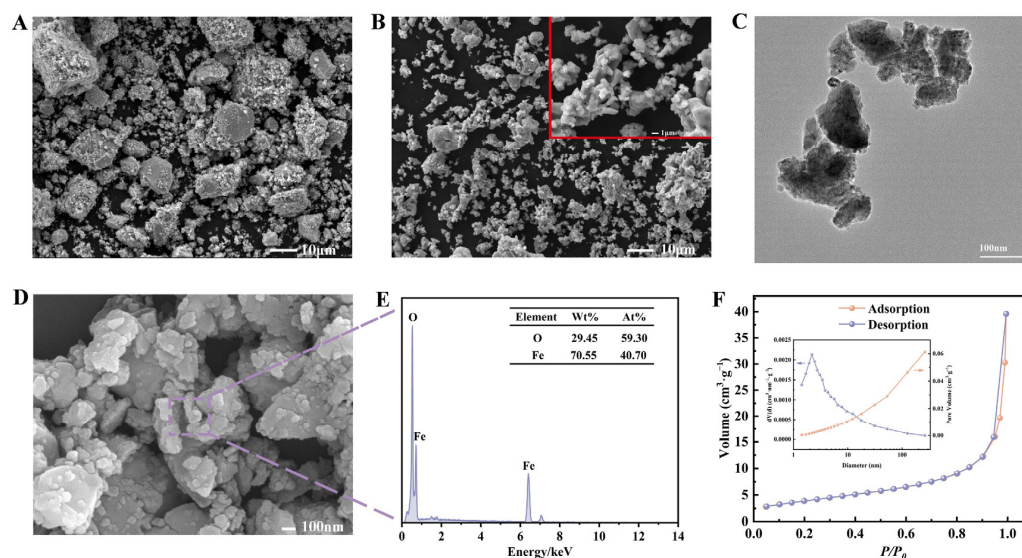


Figure 4. SEM image of (A) fine-grained pyrite and (B) calcined pyrite, (C) TEM image, (D) SEM image, (E) EDS analysis, and (F) N_2 adsorption–desorption isotherms and Barrett–Joyner–Halenda plot of Fe_2O_3 NPs.

3.2. Factors Affecting the Adsorption Efficiency of RE^{3+}

3.2.1. Time

Figure 5A depicts the correlation between the adsorption efficiency of RE^{3+} by Fe_2O_3 NPs and the adsorption time. The results showed that the adsorption of RE^{3+} was rapid within the first 10 min, attributed to the abundance of active sites available on the adsor-

bent surface [16]. Subsequently, the adsorption efficiency gradually decreased due to the reduction in active sites and the weakening of the driving force, reaching equilibrium in approximately 60 min. Based on these findings, an optimal adsorption time of 60 min was determined for subsequent experiments.

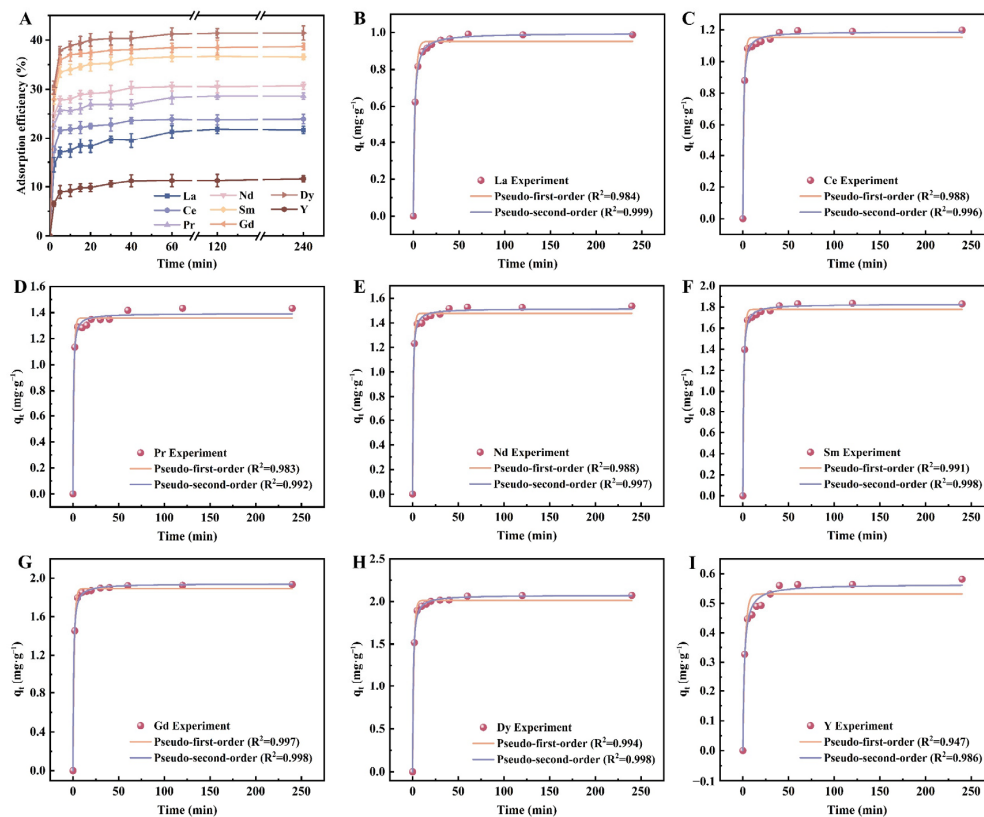


Figure 5. (A) Effect of adsorption time on the adsorption of RE³⁺ by Fe₂O₃ NPs and (B–I) pseudo-first-order and pseudo-second-order fitting of the adsorption data on Fe₂O₃ NPs (experimental conditions: initial RE³⁺ concentration = 5 mg·L^{−1}, adsorbent dosage = 50 mg, adsorption time = 0–240 min, 298 K, pH = 5.0, V = 50 mL).

To further understand the adsorption kinetics of RE³⁺ on the Fe₂O₃ NPs, the results of the batch experiments were fitted with two classical models: the pseudo-first-order (PFO) model (Equation (3)) and the pseudo-second-order (PSO) model (Equation (4)) [41].

$$\ln(q_e - q_t) = \ln q_e - k_1 t \tag{3}$$

$$\frac{t}{q_t} = \frac{1}{k_2 q_e^2} + \frac{t}{q_e} \tag{4}$$

where k_1 (min^{−1}) and k_2 (g·mg^{−1}·min^{−1}) denote the pseudo-first-order and pseudo-second-order kinetic rate constants, respectively.

Figure 5B–I illustrates the nonlinear fit of the PFO and PSO models to the adsorption of RE³⁺ on the Fe₂O₃ NPs, and the kinetic parameters are summarized in Table 3. The correlation coefficient (R^2) values clearly indicated that the adsorption kinetics of RE³⁺ on the Fe₂O₃ NPs could be more accurately explained by the PSO kinetic model. Furthermore, the experimental values of q_e ($q_{e,exp}$) were in close agreement with the theoretical values of q_e ($q_{e,cal}$) calculated by the PSO model. This suggested that the adsorption efficiency limiting step was a chemisorption process through electron sharing or exchange between the Fe₂O₃ NPs and RE³⁺ [42].

Table 3. Kinetic parameters for the adsorption of RE³⁺ onto Fe₂O₃ NPs.

Ions	$q_{e,exp}/$ ($\text{mg}\cdot\text{g}^{-1}$)	Pseudo-First Order			Pseudo-Second Order		
		$q_{e,cal}/$ ($\text{mg}\cdot\text{g}^{-1}$)	$k_1/$ min^{-1}	R ²	$q_{e,cal}/$ ($\text{mg}\cdot\text{g}^{-1}$)	$k_2/$ $\text{g}\cdot\text{mg}^{-1}\cdot\text{min}^{-1}$	R ²
La ³⁺	0.99	0.95	0.48	0.984	1.00	0.85	0.999
Ce ³⁺	1.19	1.15	0.70	0.988	1.19	1.23	0.996
Pr ³⁺	1.43	1.36	0.88	0.983	1.39	1.47	0.992
Nd ³⁺	1.53	1.48	0.87	0.988	1.51	1.36	0.997
Sm ³⁺	1.83	1.78	0.75	0.991	1.83	0.91	0.998
Gd ³⁺	1.93	1.89	0.72	0.997	1.94	0.84	0.998
Dy ³⁺	2.07	2.01	0.68	0.994	2.08	0.71	0.998
Y ³⁺	0.58	0.53	0.42	0.947	0.56	1.12	0.986

3.2.2. pH

The pH of the solution can affect the adsorption capacity of the adsorbent by affecting the activity of functional groups and the surface charge [43]. Therefore, the adsorption efficiencies of the Fe₂O₃ NPs for mixed RE³⁺ at various pH values were investigated and are shown in Figure 6A. The results revealed that the adsorption efficiency of RE³⁺ by the Fe₂O₃ NPs increased as the initial pH of the solution increased, reaching 100% at pH 7.0. The isoelectric point of the Fe₂O₃ NPs was found to be 5.64 (Figure 6B). At lower pH values, the functional groups on the surface of the Fe₂O₃ NPs became protonated and positively charged, leading to competition between H⁺ and RE³⁺ for active sites on the adsorbent surface, thereby hindering the adsorption of RE³⁺ [16]. This resulted in lower adsorption efficiencies. As the pH increased, the positive charge on the surface of the Fe₂O₃ NPs decreased gradually and became negatively charged at pH > 5.64 (Figure 6B). This resulted in electrostatic attraction between the Fe₂O₃ NPs and RE³⁺, increasing the adsorption efficiency of RE³⁺ [29]. The adsorption efficiency reached 100% rapidly at pH 7.0. Notably, pH also influences the distribution of RE³⁺ species in the solution [2]. Hence, the distribution of RE³⁺ species at thermodynamic equilibrium was calculated using Visual MINTEQ [29], and the results are shown in Figure 7. It was observed that in different pH ranges, RE³⁺ existed as different species, including RE³⁺, RE(OH)²⁺, and RE(OH)_{3(s)} [2]. The precipitation of RE(OH)_{3(s)} began at pH values of 8.2, 8.2, 8.0, 7.4, 6.8, 6.4, 6.8, and 7.4 for La³⁺, Ce³⁺, Pr³⁺, Nd³⁺, Sm³⁺, Gd³⁺, Dy³⁺, and Y³⁺, respectively. In solutions with pH ≤ 6.0, RE³⁺ was the dominant species. This conclusion is in agreement with previous research [2]. Therefore, a pH of 6.0 was identified as the optimal pH because it achieved a high adsorption efficiency and prevented the precipitation of RE(OH)_{3(s)}.

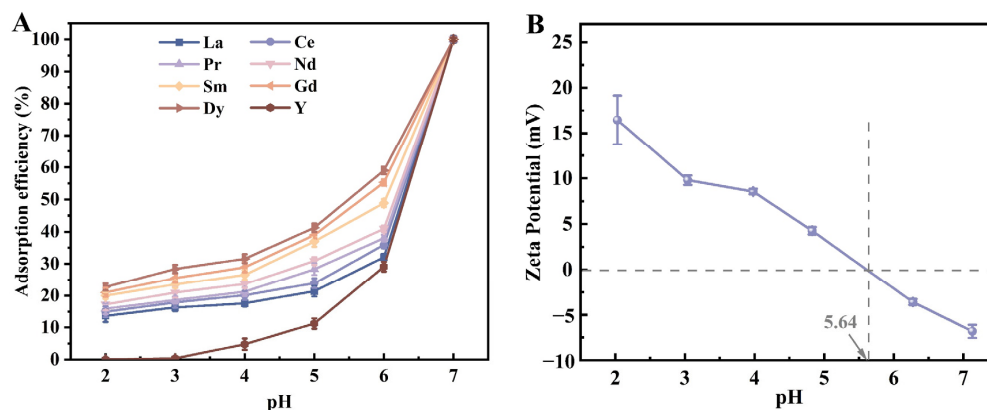


Figure 6. (A) Effect of pH on the adsorption of RE³⁺ by Fe₂O₃ NPs (experimental conditions: initial RE³⁺ concentration = 5 mg·L⁻¹, adsorbent dosage = 50 mg, adsorption time = 60 min, 298 K, pH = 2.0–7.0, V = 50 mL) and (B) Zeta potential of Fe₂O₃ NPs before the adsorption of RE³⁺.

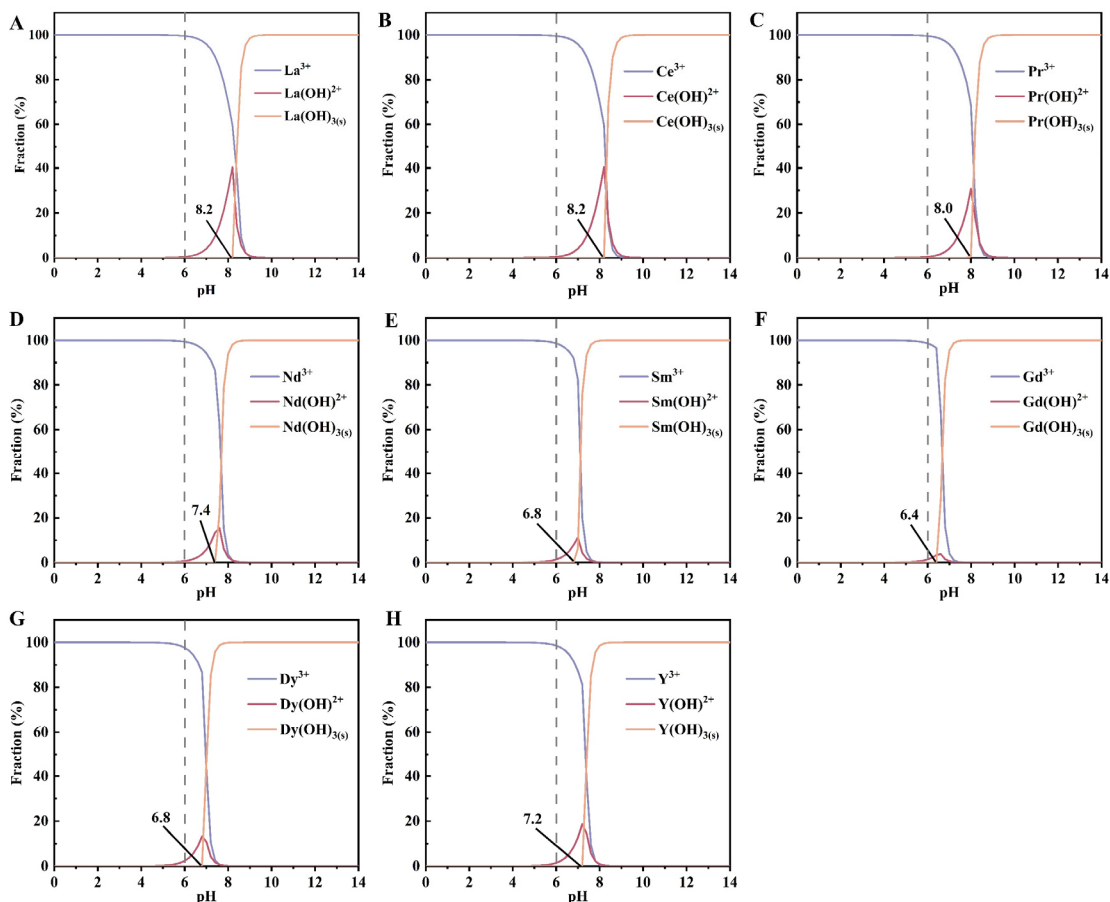


Figure 7. Distribution of hydrolysis products of RE^{3+} in aqueous solutions: (A) La^{3+} , (B) Ce^{3+} , (C) Pr^{3+} , (D) Nd^{3+} , (E) Sm^{3+} , (F) Gd^{3+} , (G) Dy^{3+} , (H) Y^{3+} (experimental conditions: initial RE^{3+} concentration = $5 \text{ mg}\cdot\text{L}^{-1}$, 298 K).

3.2.3. Initial RE^{3+} Concentration

The equilibrium adsorption capacity increased with RE^{3+} concentration, as shown in Figure 8A. This could be attributed to the greater driving force at higher initial ion concentrations, which facilitated overcoming the mass transfer resistance between the solid and liquid phases [16]. Consequently, more interactions occurred between RE^{3+} and the active sites of the adsorbent, leading to a higher adsorption capacity. This finding was consistent with previous research [11].

Two well-known isotherm models, the Langmuir (Equation (5)) and Freundlich (Equation (6)) models [11], were utilized to analyze the experimental data. The dimensionless separation factor R_L (Equation (7)) was also employed to assess the affinity between the adsorbent and RE^{3+} [17]. The Langmuir model demonstrated higher correlation coefficients ($0.990 < R^2 < 0.994$) compared to the Freundlich model (Figure 8B–I and Table 4), indicating better agreement with the experimental data. This suggested that the adsorption of RE^{3+} on the Fe_2O_3 NPs was a monolayer adsorption [9]. Once the active sites were covered by ions, no further adsorption occurred. Moreover, the positive K_L values for all eight types of RE^{3+} resulted in R_L values between 0 and 1, indicating that the adsorption process of RE^{3+} on Fe_2O_3 NPs was favorable [12]. According to the Langmuir isotherm model, the maximum adsorption capacities of the Fe_2O_3 NPs for La^{3+} , Ce^{3+} , Pr^{3+} , Nd^{3+} , Sm^{3+} , Gd^{3+} , Dy^{3+} , and Y^{3+} were calculated to be 12.80, 14.02, 14.67, 15.52, 17.66, 19.16, 19.94, and 11.82 $\text{mg}\cdot\text{g}^{-1}$, respectively. The adsorption capacities of the Fe_2O_3 NPs for RE^{3+} decreased in the order of $\text{Dy}^{3+} > \text{Gd}^{3+} > \text{Sm}^{3+} > \text{Nd}^{3+} > \text{Pr}^{3+} > \text{Ce}^{3+} > \text{La}^{3+} > \text{Y}^{3+}$, corresponding to the increasing radius of RE^{3+} [44], except for Y^{3+} . This might be due to the different electronic configuration of Y^{3+} compared to other lanthanide ions [45]. Furthermore, compared with the adsorption

capacities of RE³⁺ by different iron oxides adsorbents reported in the literature (Table 5), the Fe₂O₃ NPs synthesized in this study exhibit competitive advantages in the adsorption of RE³⁺ [41,46].

$$\frac{C_e}{q_e} = \frac{C_e}{q_m} + \frac{1}{K_L q_m} \tag{5}$$

$$\ln q_e = \ln K_F + \frac{1}{n} \ln C_e \tag{6}$$

$$R_L = \frac{1}{(1 + K_L C_0)} \tag{7}$$

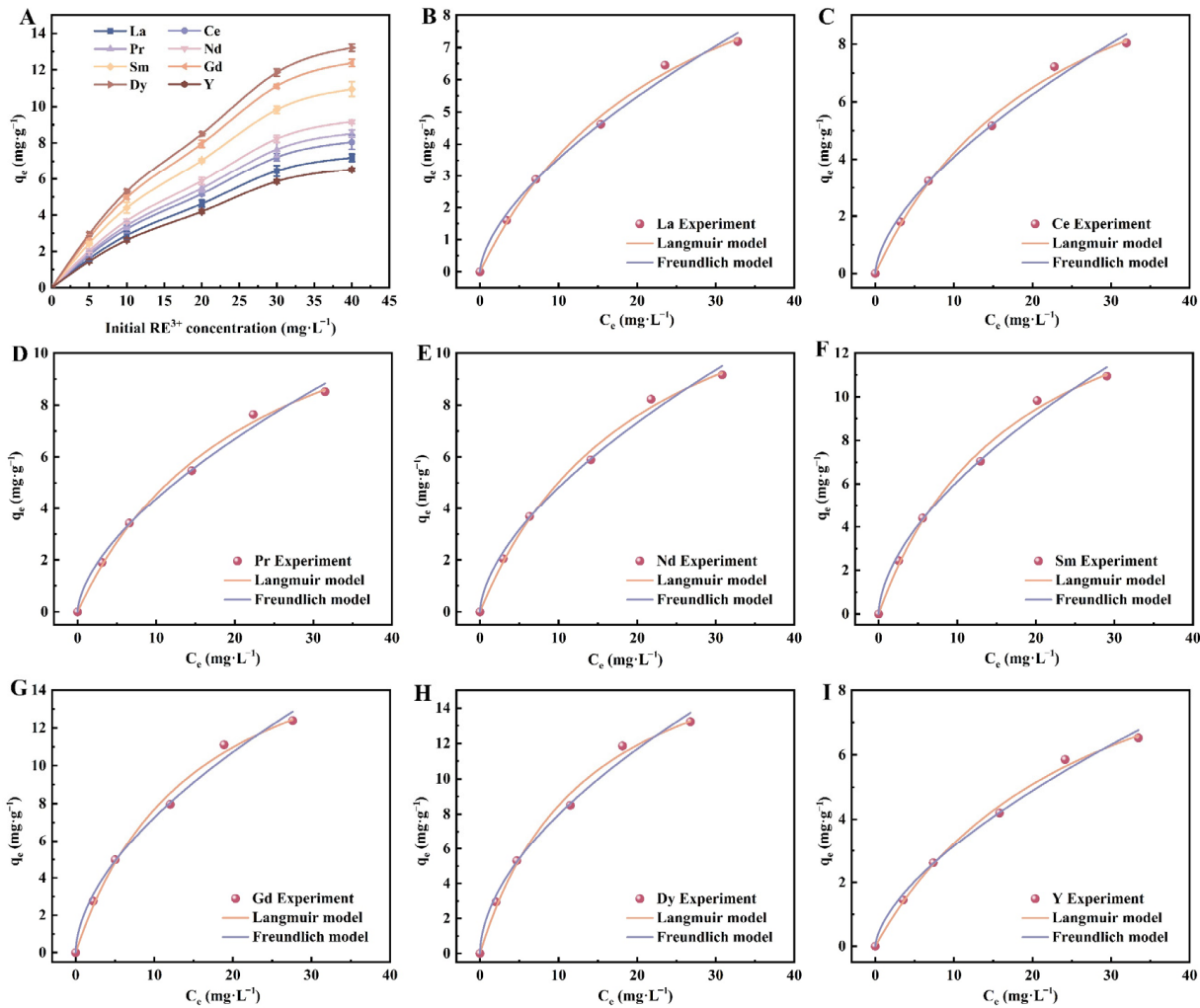


Figure 8. (A) Effect of initial RE³⁺ concentration on the adsorption of RE³⁺ by Fe₂O₃ NPs and (B–I) the adsorption data of RE³⁺ onto Fe₂O₃ NPs fitting by Langmuir and Freundlich isotherm models (experimental conditions: initial RE³⁺ concentration = 5–40 mg·L⁻¹, adsorbent dosage = 50 mg, V = 50 mL, adsorption time = 60 min, pH = 6.0, 298 K).

where q_m (mg·g⁻¹) is the maximum adsorption capacity, K_L (L·mg⁻¹) and K_F (mg·g⁻¹) represent the adsorption constants of the Langmuir and Freundlich models, respectively, and n denotes adsorption intensity [16].

Table 4. Adsorption isotherm constants for RE³⁺ adsorption on Fe₂O₃ NPs.

REEs	Langmuir Constants			Freundlich Constants		
	q _m /(mg·g ⁻¹)	k _L /(L·mg ⁻¹)	R ²	K _F /(mg·g ⁻¹)	1/n	R ²
La	12.804	0.040	0.992	0.840	0.625	0.991
Ce	14.023	0.043	0.993	0.986	0.617	0.991
Pr	14.665	0.045	0.991	1.072	0.612	0.990
Nd	15.520	0.048	0.992	1.198	0.604	0.991
Sm	17.659	0.057	0.990	1.595	0.583	0.988
Gd	19.160	0.067	0.991	1.980	0.564	0.990
Dy	19.940	0.074	0.990	2.237	0.552	0.986
Y	11.816	0.038	0.994	0.736	0.632	0.991

Table 5. Reported literature review of mixed RE³⁺ adsorption capacities by different iron oxide adsorbents.

Adsorbents	Ions	Adsorption Capacity (mg·g ⁻¹)	Ref.
Hollow core/shell hematite microspheres	Sm	14.48	[41]
Functionalized Fe ₃ O ₄ NPs	La, Nd, Gd, Y	32.5, 41.0, 52.0, 35.8	[17]
Calcium alginate/carboxymethyl chitosan/Ni _{0.2} Zn _{0.2} Fe _{2.6} O ₄	Nd, Tb, Dy	23.15, 24.41, 25.24	[47]
Magnetite nanoparticles functionalized with organophosphorus compounds	La, Pr, Nd	8.3, 8.7, 8.9	[46]
Fe ₂ O ₃ NPs (this work)	La, Ce, Pr, Nd, Sm, Gd, Dy, Y	12.8, 14.0, 14.7, 15.5, 17.7, 19.2, 19.9, 11.8	

3.2.4. Temperature

The adsorption of metal ions at the solid–liquid interface was influenced by thermodynamic interactions between molecules [25]. To understand the energy change in Fe₂O₃ NPs adsorbing RE³⁺, the thermodynamic behavior was investigated [9]. As illustrated in Figure 9, the adsorption efficiency of all RE³⁺ increased with temperature, which could be attributed to the increased mobility of metal ions [16]. The thermodynamic parameters such as Gibbs free energy (ΔG⁰), enthalpy (ΔH⁰), and entropy (ΔS⁰) were calculated using Equations (8)–(10) [16]. The thermodynamic parameters at different temperatures, presented in Table 6, revealed that the ΔG⁰ values for La³⁺, Ce³⁺, Pr³⁺, Nd³⁺, Sm³⁺, and Y³⁺ were positive, indicating non-spontaneous adsorption at room temperature. However, at higher temperatures, ΔG⁰ for Sm³⁺ became negative, suggesting spontaneous adsorption. Gd³⁺ and Dy³⁺ exhibited negative ΔG⁰ values within the tested temperature range, indicating spontaneous adsorption on the Fe₂O₃ NPs. Particularly, the ΔG⁰ value for Dy³⁺ was more negative, suggesting stronger adsorption feasibility [16]. As the temperature increased from 298 K to 318 K, the negative ΔG⁰ values became larger, and the positive ΔG⁰ values became smaller for all eight types of RE³⁺, indicating that higher temperatures could enhance adsorption efficiency [9]. The positive ΔH⁰ value suggested that the adsorption process of RE³⁺ on the Fe₂O₃ NPs was endothermic [9]. Additionally, the positive ΔS⁰ value indicated that the randomness and disorder of the solid–solution interface increased during the adsorption process of RE³⁺ on the Fe₂O₃ NPs [16].

$$K_d = \frac{q_e}{C_e} \tag{8}$$

$$\ln K_d = \frac{\Delta S^0}{R} - \frac{\Delta H^0}{RT} \tag{9}$$

$$\Delta G^0 = -RT \ln K_d = \Delta H^0 - T \Delta S^0 \tag{10}$$

where R stands for the gas constant ($8.314 \text{ J}\cdot\text{mol}^{-1}\cdot\text{K}^{-1}$), T (K) is the absolute temperature, and K_d represents the distribution coefficient.

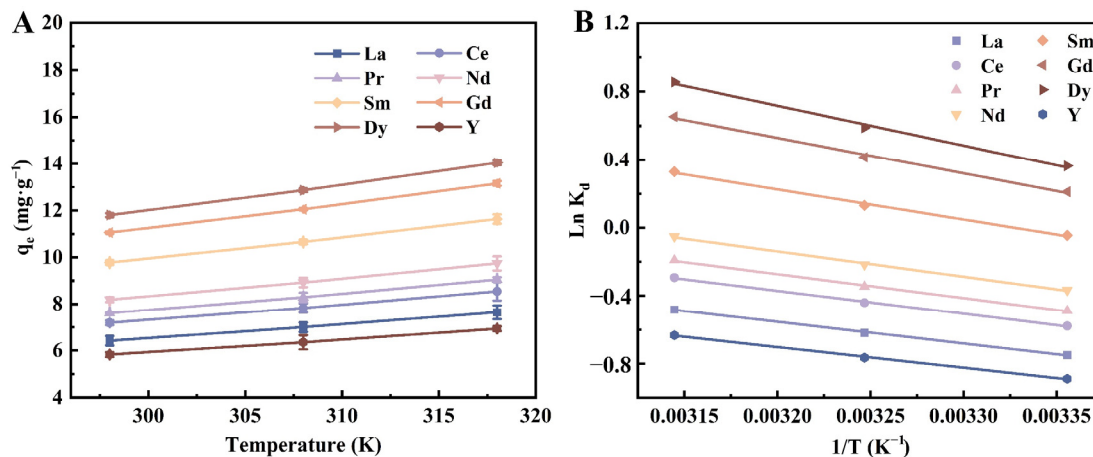


Figure 9. (A) Effect of temperature on the adsorption of RE³⁺ by Fe₂O₃ NPs and (B) linear plot of $\ln K_d$ versus $1/T$ for adsorption capacity of RE³⁺ on Fe₂O₃ NPs (experimental conditions: initial RE³⁺ concentration = 20 mg·L⁻¹, adsorbent dosage = 50 mg, T = 60 min, V = 50 mL, pH = 6.0).

Table 6. Thermodynamic parameters for the adsorption of RE³⁺ by Fe₂O₃ NPs at 298–318 K.

RE ³⁺	ΔG^0 (kJ·mol ⁻¹)			ΔH^0 (kJ·mol ⁻¹)	ΔS^0 (J·mol ⁻¹ ·K ⁻¹)	R ²
	298K	308K	318K			
La	1.857	1.588	1.274	10.551	29.149	0.997
Ce	1.435	1.130	0.774	11.278	33.002	0.997
Pr	1.212	0.886	0.506	11.723	35.243	0.997
Nd	0.910	0.555	0.138	12.400	38.525	0.996
Sm	0.111	-0.336	-0.871	14.735	49.027	0.994
Gd	-0.525	-1.065	-1.728	17.378	60.012	0.992
Dy	-0.902	-1.508	-2.267	19.413	68.091	0.990
Y	2.202	1.959	1.675	10.050	26.313	0.997

3.3. Selective Separation

To investigate the selective adsorption of RE³⁺ on the Fe₂O₃ NPs, Gd³⁺ and Dy³⁺ were chosen as representatives. The separation factors (SF) (Equation (11)) for these two ions were calculated and compared (Table 7) [17,48]. The results showed the successful separation of Gd³⁺ and Dy³⁺ by the Fe₂O₃ NPs in a solution with eight types of mixed RE³⁺. The separation selectivity, reflected in the SF values, increased with the distance between the two REEs, suggesting that the difference in size between the ions played a role in the high separation selectivity [17]. Additionally, Gd³⁺ and Dy³⁺ could be easily separated from solutions containing Y³⁺. Notably, the Fe₂O₃ NPs exhibited a higher selectivity for Dy³⁺ separation compared to Gd³⁺, possibly due to the smaller ionic radius of Dy³⁺, which facilitated its binding to active sites on the surface of the Fe₂O₃ NPs.

$$SF(A/B) = \frac{K_d(A)}{K_d(B)} \tag{11}$$

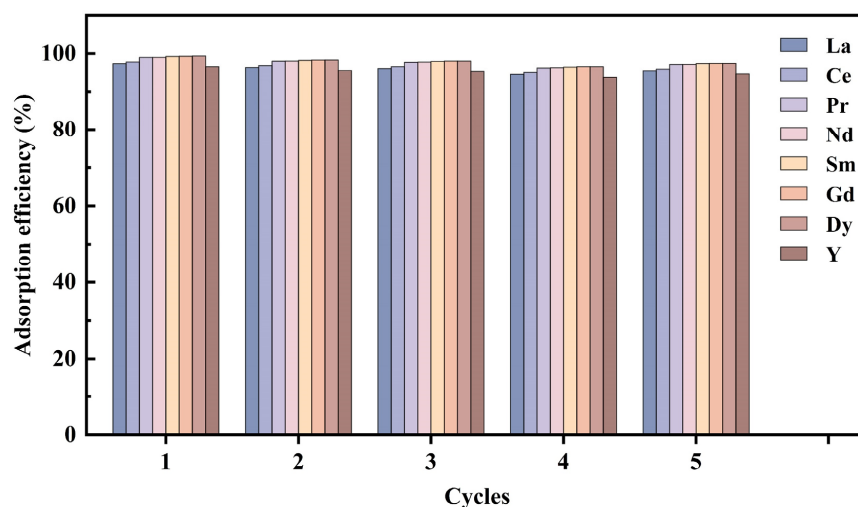
where K_d is the adsorption partition coefficient; $K_d(A)$ and $K_d(B)$ denote the K_d values of A and B ions, respectively; and $SF(A/B)$ is the separation coefficient of A and B ions.

Table 7. Selective separation factors (SF) of Gd³⁺ and Dy³⁺ from the mixed RE³⁺ solutions using Fe₂O₃ NPs.

SF	298K	308K	318K	SF	298K	308K	318K
Gd ³⁺ /La ³⁺	2.62	2.82	3.11	Dy ³⁺ /La ³⁺	3.05	3.35	3.82
Gd ³⁺ /Ce ³⁺	2.21	2.36	2.58	Dy ³⁺ /Ce ³⁺	2.57	2.80	3.16
Gd ³⁺ /Pr ³⁺	2.02	2.14	2.33	Dy ³⁺ /Pr ³⁺	2.35	2.55	2.85
Gd ³⁺ /Nd ³⁺	1.78	1.88	2.03	Dy ³⁺ /Nd ³⁺	2.08	2.24	2.48
Gd ³⁺ /Sm ³⁺	1.29	1.33	1.38	Dy ³⁺ /Sm ³⁺	1.51	1.58	1.70
Gd ³⁺ /Dy ³⁺	0.86	0.84	0.82	Dy ³⁺ /Gd ³⁺	1.16	1.19	1.23
Gd ³⁺ /Y ³⁺	3.01	3.26	3.62	Dy ³⁺ /Y ³⁺	3.50	3.87	4.44

3.4. Reusability

The reusability of adsorbents is essential for their practical application [9]. Figure 10 displays the results for the adsorption efficiency of RE³⁺ on the Fe₂O₃ NPs as the number of adsorption–desorption cycles increases. In the first cycle, the adsorption efficiencies of the Fe₂O₃ NPs for the eight types of RE³⁺ were 97.32%, 97.81%, 98.99%, 99.03%, 99.24%, 99.30%, 99.32%, and 96.53%, respectively. After five adsorption–desorption cycles, a slight decrease in adsorption efficiency was observed, with 95.47%, 95.95%, 97.11%, 97.15%, 97.36%, 97.42%, 97.43%, and 94.70%, respectively. This slight decrease could be attributed to the incomplete release of RE³⁺ from the adsorption sites during the desorption process, leading to the deactivation of some surface sites [16]. These findings indicated that Fe₂O₃ NPs could be considered as a reusable and recyclable adsorbent for RE³⁺.

**Figure 10.** Reusability of Fe₂O₃ NPs for adsorption of RE³⁺ (experimental conditions: initial RE³⁺ concentration = 5 mg·L⁻¹, adsorbent dosage = 100 mg, T = 60 min, V = 50 mL, pH = 6.0, 298 K).

3.5. Application of Fe₂O₃ NPs to Actual Mine Wastewater

In actual rare earth mine wastewater, RE³⁺ commonly co-exists with transition metal and alkaline earth ions, which may interfere with the adsorption of RE³⁺ [11]. Therefore, the adsorption efficiency of Fe₂O₃ NPs for RE³⁺ in the actual mine wastewater was investigated (Figure 11). The main components of metal ions in the mine wastewater are listed in Table 1. After treatment, the adsorption efficiency of all RE³⁺ in the mine wastewater was found to be above 90.5%, indicating that Fe₂O₃ NPs effectively adsorb RE³⁺ from the actual mine wastewater. Moreover, adsorption efficiencies for Ca²⁺ (4.9%), K⁺ (10.3%), Na⁺ (3.7%), Mg²⁺ (11.5%), Al³⁺ (17.5%), and Mn²⁺ (23.7%) were low. Evidently, Fe₂O₃ NPs exhibited a superior adsorption of RE³⁺ compared to other metal ions. This could be explained by the fact that the binding of RE³⁺ to the O donor atoms was stronger than that of the common interfering ions [17].

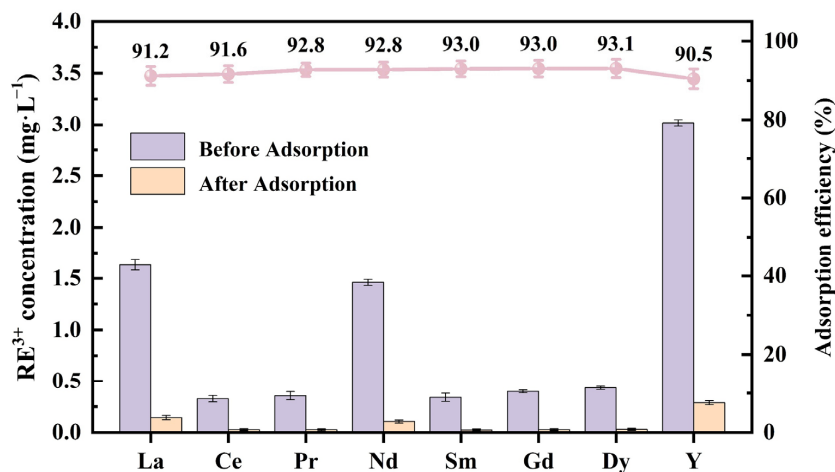


Figure 11. Adsorption of Fe₂O₃ NPs for RE³⁺ in rare earth mine wastewater.

3.6. Adsorption Mechanism

The morphology and elemental composition of the Fe₂O₃ NPs before and after the adsorption of RE³⁺ were investigated using SEM. SEM images revealed that there were more small particles on the surface of the Fe₂O₃ NPs after adsorbing RE³⁺ (Figure 12A) compared to the original Fe₂O₃ NPs (Figure 4D), possibly due to magnetic stirring during adsorption. EDS analysis (Figure 12B) and the full XPS spectrum (Figure 12C) confirmed the presence of REEs on the surface of the Fe₂O₃ NPs, providing evidence for the adsorption of RE³⁺. Furthermore, the elemental mapping of the Fe₂O₃ NPs loaded with RE³⁺ demonstrated that RE³⁺ was uniformly adsorbed on the surface of the Fe₂O₃ NPs (Figure S2).

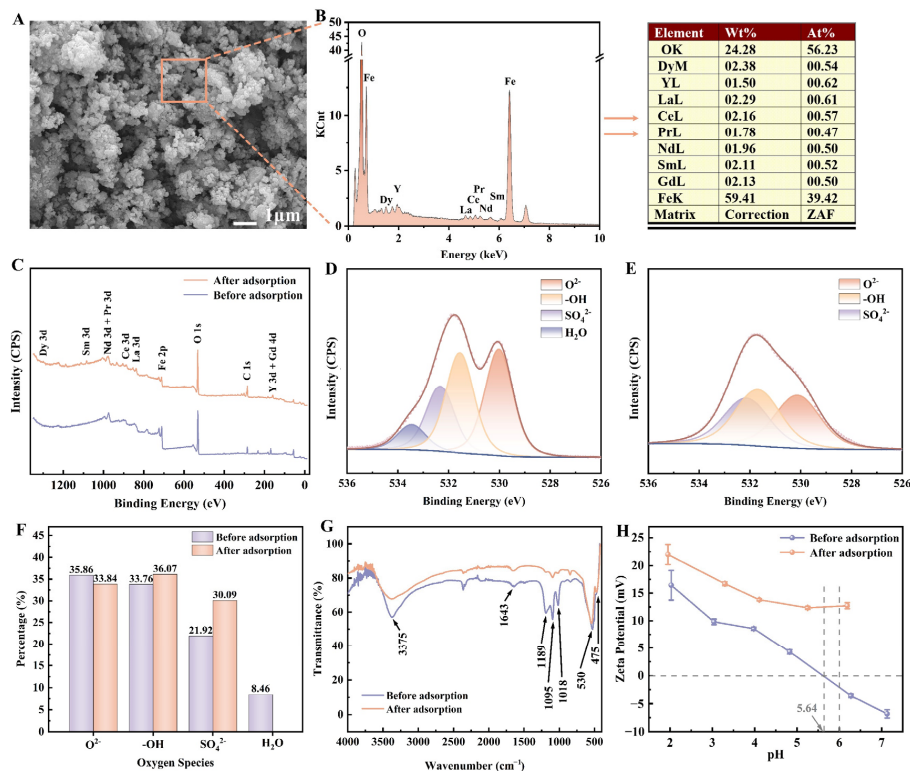


Figure 12. (A) SEM image and (B) EDS spectra of Fe₂O₃ NPs after the adsorption of RE³⁺, (C) full-range survey XPS spectrum of Fe₂O₃ NPs before and after the adsorption of RE³⁺, XPS spectra of the O 1s peak of Fe₂O₃ NPs (D) before and (E) after the adsorption of RE³⁺, (F) contents of different oxygen species on the Fe₂O₃ NPs surface (atom%), (G) FTIR spectra and (H) zeta potential of Fe₂O₃ NPs before and after the adsorption of RE³⁺.

The O 1s peaks before and after RE^{3+} adsorption on the Fe_2O_3 NPs are shown in Figure 12D,E. The O 1s spectrum of the Fe_2O_3 NPs could be deconvoluted into four peaks located at approximately 530.0, 531.5, 532.3, and 533.5 eV, which corresponded to oxygen atoms bonded to iron atoms (Fe-O), surface hydroxyl (Fe-OH), Fe- SO_4 , and adsorbed water (H_2O), respectively [23]. The presence of Fe- SO_4 was attributed to residual iron sulfate on the surface of Fe_2O_3 NPs, formed after the calcination of pyrite. After the adsorption of RE^{3+} , the surface oxygen content of the Fe_2O_3 NPs decreased slightly. Furthermore, the Fe-O content decreased from 35.86% to 33.84%, while the Fe-OH and Fe- SO_4 contents increased from 33.76% and 21.92% to 36.07% and 30.09%, respectively (Figure 12F). These findings suggested that the O-groups on the surface of Fe_2O_3 NPs were consumed by binding to RE^{3+} during adsorption.

Figure 12G presents the FTIR spectra of the Fe_2O_3 NPs before and after the adsorption of RE^{3+} . The absorption band at 3375 cm^{-1} was attributed to the stretching vibrations of -OH, and the peak at 1643 cm^{-1} corresponded to the deformation of the H_2O molecule. The absorption bands observed at 1189 and 1095 cm^{-1} were attributed to the double vibration of SO_4^{2-} [49], which aligned with the XPS results (Figure 12D,E). Additionally, the fluctuation at 1018 cm^{-1} represented the in-plane bending vibration of -OH, and the absorption peaks at 475 and 530 cm^{-1} were related to the tensile vibration of Fe-O [22]. After the adsorption of RE^{3+} , the intensity of the -OH and SO_4^{2-} absorption bands on the surface of the Fe_2O_3 NPs decreased significantly, demonstrating the substantial contribution of -OH and SO_4^{2-} to the adsorption process. The adsorption of RE^{3+} by -OH and SO_4^{2-} could be explained by the surface complexation mechanism, which was consistent with the hard-soft acid-base (HSAB) theory. According to HSAB theory, hard acids, such as RE^{3+} , tend to form strong ionic complexes with hard bases like O^- , OH^- , and SO_4^{2-} [50,51]. Moreover, at a high pH, -OH ionized to O^- , which, together with the O^- presented in the Fe_2O_3 NPs itself, absorbed RE^{3+} by forming a complex. In addition, no Fe^{3+} was detected in the solution after adsorption, suggesting that the adsorption mechanism did not involve ion exchanges between Fe^{3+} and RE^{3+} .

Zeta potential measurements were conducted to examine the presence of electrostatic attraction during the adsorption process [29]. Figure 12H shows that as the pH increased, the concentration of OH^- also increased, leading to a decrease in the Zeta potential of Fe_2O_3 NPs [52]. The zero potential value of the Fe_2O_3 NPs was -2.17 mV at pH 6.0. However, after the adsorption of RE^{3+} , the zeta potential increased to 12.73 mV , indicating the occurrence of charge neutralization in the adsorption process, and electrostatic attraction was one of the reasons for the adsorption [11]. Therefore, the use of pyrite calcination to prepare Fe_2O_3 NPs as an adsorbent offered multiple advantages, including electrostatic adsorption, the complexation of RE^{3+} by -OH and O^- , and the presence of additional SO_4^{2-} adsorption sites due to the incomplete thermal decomposition of the pyrite surface. Based on these findings, a schematic diagram of the adsorption mechanism of Fe_2O_3 NPs for RE^{3+} was proposed (Figure 13).

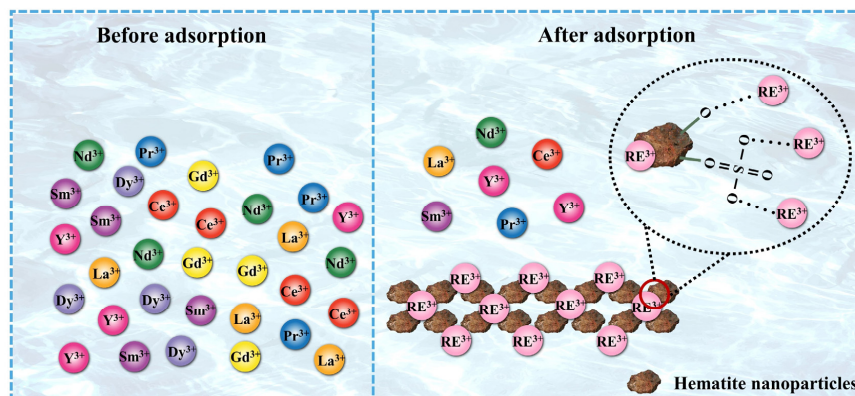


Figure 13. Schematic diagram of the adsorption mechanism of Fe_2O_3 NPs for RE^{3+} .

4. Conclusions

In this study, Fe₂O₃ NPs were successfully synthesized from natural pyrite through a high-temperature phase transition to adsorb mixed RE³⁺ from mine wastewater. The optimal time and pH for the adsorption of RE³⁺ by Fe₂O₃ NPs were 60 min and 6.0, respectively. The maximum adsorption capacities for La³⁺, Ce³⁺, Pr³⁺, Nd³⁺, Sm³⁺, Gd³⁺, Dy³⁺, and Y³⁺ were 12.80, 14.02, 14.67, 15.52, 17.66, 19.16, 19.94, and 11.82 mg·g⁻¹, respectively. Fe₂O₃ NPs exhibited a stronger affinity for Gd³⁺ and Dy³⁺, enabling the effective separation of these ions from the mixed RE³⁺ aqueous solution. Compared to iron oxides adsorbents synthesized using chemical reagents reported in the literature, Fe₂O₃ NPs demonstrated competitive advantages. The adsorption process was characterized by monolayer chemisorption, which was achieved by surface complexation and electrostatic attraction. After five adsorption–desorption cycles, the removal efficiency of RE³⁺ remained above 94.7%, indicating the reusability of Fe₂O₃ NPs. Furthermore, Fe₂O₃ NPs effectively adsorbed RE³⁺ from actual mine wastewater, even in the presence of high concentrations of transition metal and alkaline earth ions. Therefore, Fe₂O₃ NPs, as a simple, reusable, and easily separable adsorbent, show significant potential for the adsorption of RE³⁺ from actual mine wastewater. This study provided a strategy for the recovery and removal of RE³⁺ from aqueous solutions and the resource utilization of pyrite. Future research could focus on developing eluents with specific selectivity to improve the purity of rare earth elements.

Supplementary Materials: The following supporting information can be downloaded at: <https://www.mdpi.com/article/10.3390/min14050464/s1>, Figure S1: XRD pattern of pyrite; Figure S2: SEM-Mapping images of Fe₂O₃ NPs after adsorption of RE³⁺; Table S1: Different levels and factors of the orthogonal experiments on the grinding process of pyrite; Table S2: Parameters of the orthogonal experiments on the grinding process of pyrite.

Author Contributions: C.Z.: Investigation, data analysis, interpretation of results, and writing—original draft. J.W.: resources, funding acquisition, and project administration. B.Y.: writing—review and editing. Y.L.: writing—review and editing and project administration. G.Q.: resources and conceptualization. All authors have read and agreed to the published version of the manuscript.

Funding: This work was supported by the National Key Research and Development Program of China (No. 2022YFC2105300), the National Natural Science Foundation of China (No. 52274288), and Central South University Innovation-Driven Research Program (No. 2023CXQD070).

Data Availability Statement: All data are provided within the article and Supplementary Materials.

Conflicts of Interest: The authors declare no conflict of interest.

References

1. Yang, Y.; Weng, X.; Chen, Z. Recovery of rare earth elements from mine wastewater using biosynthesized reduced graphene oxide. *J. Colloid Interface Sci.* **2023**, *638*, 449–460. [[CrossRef](#)] [[PubMed](#)]
2. Cui, J.; Wang, Q.; Gao, J.; Guo, Y.; Cheng, F. The selective adsorption of rare earth elements by modified coal fly ash based SBA-15. *Chin. J. Chem. Eng.* **2022**, *47*, 155–164. [[CrossRef](#)]
3. Liu, C.; Liu, W.S.; Huot, H.; Guo, M.N.; Zhu, S.C.; Zheng, H.X.; Morel, J.L.; Tang, Y.T.; Qiu, R.L. Biogeochemical cycles of nutrients, rare earth elements (REEs) and Al in soil-plant system in ion-adsorption REE mine tailings remediated with amendment and ramie (*Boehmeria nivea* L.). *Sci. Total Environ.* **2022**, *809*, 152075. [[CrossRef](#)] [[PubMed](#)]
4. Xie, X.; Tan, X.; Yu, Y.; Li, Y.; Wang, P.; Liang, Y.; Yan, Y. Effectively auto-regulated adsorption and recovery of rare earth elements via an engineered *E. coli*. *J. Hazard. Mater.* **2022**, *424 Pt C*, 127642. [[CrossRef](#)]
5. Guo, Z.; Li, Q.; Li, Z.; Liu, C.; Liu, X.; Liu, Y.; Dong, G.; Lan, T.; Wei, Y. Fabrication of efficient alginate composite beads embedded with N-doped carbon dots and their application for enhanced rare earth elements adsorption from aqueous solutions. *J. Colloid Interface Sci.* **2020**, *562*, 224–234. [[CrossRef](#)] [[PubMed](#)]
6. Iftekhhar, S.; Srivastava, V.; Hammouda, S.B.; Sillanpaa, M. Fabrication of novel metal ion imprinted xanthan gum-layered double hydroxide nanocomposite for adsorption of rare earth elements. *Carbohydr. Polym.* **2018**, *194*, 274–284. [[CrossRef](#)]
7. Wang, Y.; Wang, G.; Sun, M.; Liang, X.; He, H.; Zhu, J.; Takahashi, Y. Environmental risk assessment of the potential “Chemical Time Bomb” of ion-adsorption type rare earth elements in urban areas. *Sci. Total Environ.* **2022**, *822*, 153305. [[CrossRef](#)] [[PubMed](#)]

8. Liu, X.-R.; Liu, W.-S.; Tang, Y.-T.; Wang, S.-Z.; Cao, Y.-J.; Chen, Z.-W.; Xie, C.-D.; Liu, C.; Guo, M.-N.; Qiu, R.-L. Effects of in situ leaching on the origin and migration of rare earth elements in aqueous systems of South China: Insights based on REE patterns, and Ce and Eu anomalies. *J. Hazard. Mater.* **2022**, *435*, 128959. [[CrossRef](#)]
9. Liu, Z.; Gao, Z.; Xu, L.; Hu, F. Efficient and rapid adsorption of rare earth elements from water by magnetic Fe₃O₄/MnO₂ decorated reduced graphene oxide. *J. Mol. Liq.* **2020**, *313*, 113510. [[CrossRef](#)]
10. Zhao, F.; Repo, E.; Meng, Y.; Wang, X.; Yin, D.; Sillanpää, M. An EDTA-β-cyclodextrin material for the adsorption of rare earth elements and its application in preconcentration of rare earth elements in seawater. *J. Colloid Interface Sci.* **2016**, *465*, 215–224. [[CrossRef](#)]
11. Xu, W.; Yu, C.; Liu, L.; Zhai, Y.; Xu, R.; Hou, H. An O- modified coordination polymer for rapid and selective adsorption of rare earth elements from aqueous solution. *Colloids Surf. A* **2020**, *607*, 125464. [[CrossRef](#)]
12. Li, J.; Gong, A.; Li, F.; Qiu, L.; Zhang, W.; Gao, G.; Liu, Y.; Li, J. Synthesis and characterization of magnetic mesoporous Fe₃O₄@mSiO₂-DODGA nanoparticles for adsorption of 16 rare earth elements. *RSC Adv.* **2018**, *8*, 39149–39161. [[CrossRef](#)] [[PubMed](#)]
13. Gomes Rodrigues, D.; Monge, S.; Pellet-Rostaing, S.; Dacheux, N.; Bouyer, D.; Faur, C. A new carbamoylmethylphosphonic acid-based polymer for the selective sorption of rare earth elements. *Chem. Eng. J.* **2019**, *371*, 857–867. [[CrossRef](#)]
14. Gomes Rodrigues, D.; Monge, S.; Pellet-Rostaing, S.; Dacheux, N.; Bouyer, D.; Faur, C. Sorption properties of carbamoylmethylphosphonated-based polymer combining both sorption and thermosensitive properties: New valuable hydrosoluble materials for rare earth elements sorption. *Chem. Eng. J.* **2019**, *355*, 871–880. [[CrossRef](#)]
15. Chen, G.E.; Sun, D.; Xu, Z.L. Rare Earth Ion from Aqueous Solution Removed by Polymer Enhanced Ultrafiltration Process. *Adv. Mater. Res.* **2011**, *233–235*, 959–964. [[CrossRef](#)]
16. Javadian, H.; Ruiz, M.; Saleh, T.A.; Sastre, A.M. Ca-alginate/carboxymethyl chitosan/Ni_{0.2}Zn_{0.2}Fe_{2.6}O₄ magnetic bionanocomposite: Synthesis, characterization and application for single adsorption of Nd⁺³, Tb⁺³, and Dy⁺³ rare earth elements from aqueous media. *J. Mol. Liq.* **2020**, *306*, 112760. [[CrossRef](#)]
17. Ashour, R.M.; El-sayed, R.; Abdel-Magied, A.F.; Abdel-khalek, A.A.; Ali, M.M.; Forsberg, K.; Uheida, A.; Muhammed, M.; Dutta, J. Selective separation of rare earth ions from aqueous solution using functionalized magnetite nanoparticles: Kinetic and thermodynamic studies. *Chem. Eng. J.* **2017**, *327*, 286–296. [[CrossRef](#)]
18. Chen, G.; Jiang, C.; Liu, R.; Xie, Z.; Liu, Z.; Cen, S.; Tao, C.; Guo, S. Leaching kinetics of manganese from pyrolusite using pyrite as a reductant under microwave heating. *Sep. Purif. Technol.* **2021**, *277*, 119472. [[CrossRef](#)]
19. Tang, J.; Zhao, B.; Lyu, H.; Li, D. Development of a novel pyrite/biochar composite (BM-FeS₂@BC) by ball milling for aqueous Cr(VI) removal and its mechanisms. *J. Hazard. Mater.* **2021**, *413*, 125415. [[CrossRef](#)]
20. Karagiorgakis, A.L.; Schindler, M.; Spiers, G.A. Retention of rare earth elements in authigenic phases following biogeochemical dissolution of ore from Elliot Lake, Ontario. *Hydrometallurgy* **2018**, *177*, 9–20. [[CrossRef](#)]
21. Li, H.; Li, Y.; Guo, J.; Song, Y.; Hou, Y.; Lu, C.; Han, Y.; Shen, X.; Liu, B. Effect of calcinated pyrite on simultaneous ammonia, nitrate and phosphorus removal in the BAF system and the Fe²⁺ regulatory mechanisms: Electron transfer and biofilm properties. *Environ. Res.* **2021**, *194*, 110708. [[CrossRef](#)] [[PubMed](#)]
22. Trang, V.T.; Tam, L.T.; Van Quy, N.; Phan, V.N.; Van Tuan, H.; Huy, T.Q.; Dinh, N.X.; Le, A.-T. Enhanced adsorption efficiency of inorganic chromium (VI) ions by using carbon-encapsulated hematite nanocubes. *J. Sci. Adv. Mater. Devices* **2020**, *5*, 392–399. [[CrossRef](#)]
23. Liang, Y.; Wang, M.; Xiong, J.; Hou, J.; Wang, X.; Tan, W. Al-substitution-induced defect sites enhance adsorption of Pb²⁺ on hematite. *Environ. Sci. Nano* **2019**, *6*, 1323–1331. [[CrossRef](#)]
24. Yuan, X.; Luo, F.; Chen, X.; Xia, W.; Zou, Y.; Zhou, X.; Liu, H.; Song, Y.; He, J.; Ma, S. Effective Cu(II) ions adsorption from aqueous solutions using low grade oolitic hematite tailing with phosphorus: Response surface methodology. *Desalination Water Treat.* **2022**, *265*, 57–70. [[CrossRef](#)]
25. Estes, S.L.; Powell, B.A. Enthalpy of Uranium Adsorption onto Hematite. *Environ. Sci. Technol.* **2020**, *54*, 15004–15012. [[CrossRef](#)] [[PubMed](#)]
26. Denys, A.; Janots, E.; Auzende, A.-L.; Lanson, M.; Findling, N.; Trcera, N. Evaluation of selectivity of sequential extraction procedure applied to REE speciation in laterite. *Chem. Geol.* **2021**, *559*, 119954. [[CrossRef](#)]
27. Viana, T.; Henriques, B.; Ferreira, N.; Pinto, R.J.B.; Monteiro, F.L.S.; Pereira, E. Insight into the mechanisms involved in the removal of toxic, rare earth, and platinum elements from complex mixtures by *Ulva* sp. *Chem. Eng. J.* **2023**, *453*, 139630. [[CrossRef](#)]
28. Zhao, C.; Yang, B.; Liao, R.; Hong, M.; Yu, S.; Liu, S.; Wang, J.; Qiu, G. Combined effect and mechanism of visible light and Ag⁺ on chalcopyrite bioleaching. *Miner. Eng.* **2022**, *175*, 107283. [[CrossRef](#)]
29. Yan, Q.; Yang, Y.; Chen, W.; Weng, X.; Owens, G.; Chen, Z. Recovery and removal of rare earth elements from mine wastewater using synthesized bio-nanoparticles derived from *Bacillus cereus*. *Chem. Eng. J.* **2023**, *459*, 141585. [[CrossRef](#)]
30. Pechishcheva, N.V.; Estemirova, S.K.; Kim, A.V.; Zaitceva, P.V.; Sterkhov, E.V.; Shchapova, Y.V.; Zhidkov, I.S.; Skrylnik, M.Y. Adsorption of hexavalent chromium on mechanically activated graphite. *Diam. Relat. Mater.* **2022**, *127*, 109152. [[CrossRef](#)]
31. El Ouardi, Y.; Lamsayah, M.; Butylina, S.; Geng, S.; Esmaili, M.; Giove, A.; Massima Mouele, E.S.; Virolainen, S.; El Barkany, S.; Ouammou, A.; et al. Sustainable composite material based on glutenin biopolymeric-clay for efficient separation of rare earth elements. *Chem. Eng. J.* **2022**, *440*, 135959. [[CrossRef](#)]

32. Ren, J.; Zheng, L.; Su, Y.; Meng, P.; Zhou, Q.; Zeng, H.; Zhang, T.; Yu, H. Competitive adsorption of Cd(II), Pb(II) and Cu(II) ions from acid mine drainage with zero-valent iron/phosphoric titanium dioxide: XPS qualitative analyses and DFT quantitative calculations. *Chem. Eng. J.* **2022**, *445*, 136778. [[CrossRef](#)]
33. Smith, Y.R.; Bhattacharyya, D.; Willhard, T.; Misra, M. Adsorption of aqueous rare earth elements using carbon black derived. *Chem. Eng. J.* **2016**, *296*, 102–111. [[CrossRef](#)]
34. Ambroz, A.; Ban, I.; Luxbacher, T. Assessment of the Capability of Magnetic Nanoparticles to Recover Neodymium Ions from Aqueous Solution. *Acta Chim. Slov.* **2022**, *69*, 826–836. [[CrossRef](#)] [[PubMed](#)]
35. He, P.; Zhu, J.; Chen, Y.; Chen, F.; Zhu, J.; Liu, M.; Zhang, K.; Gan, M. Pyrite-activated persulfate for simultaneous 2,4-DCP oxidation and Cr(VI) reduction. *Chem. Eng. J.* **2021**, *406*, 126758. [[CrossRef](#)]
36. Labus, M. Pyrite thermal decomposition in source rocks. *Fuel* **2021**, *287*, 119529. [[CrossRef](#)]
37. Abeshu, G.W.; Li, H.-Y.; Zhu, Z.; Tan, Z.; Leung, L.R. Median bed-material sediment particle size across rivers in the contiguous US. *Earth Syst. Sci. Data* **2022**, *14*, 929–942. [[CrossRef](#)]
38. Wang, Z.; Xie, X.; Xiao, S.; Liu, J. Comparative study of interaction between pyrite and cysteine by thermogravimetric and electrochemical techniques. *Hydrometallurgy* **2010**, *101*, 88–92. [[CrossRef](#)]
39. Cheng, H.; Liu, Q.; Huang, M.; Zhang, S.; Frost, R.L. Application of TG-FTIR to study SO₂ evolved during the thermal decomposition of coal-derived pyrite. *Thermochim. Acta* **2013**, *555*, 1–6. [[CrossRef](#)]
40. Yan, X.; Shao, J.; Wen, Q.; Shen, J. Stabilization of soil arsenic by natural limonite after mechanical activation and the associated mechanisms. *Sci. Total Environ.* **2020**, *708*, 135118. [[CrossRef](#)]
41. Yu, S.H.; Yao, Q.Z.; Zhou, G.T.; Fu, S.Q. Preparation of hollow core/shell microspheres of hematite and its adsorption ability for samarium. *ACS Appl. Mater. Interfaces* **2014**, *6*, 10556–10565. [[CrossRef](#)] [[PubMed](#)]
42. Tan, K.L.; Hameed, B.H. Insight into the adsorption kinetics models for the removal of contaminants from aqueous solutions. *J. Taiwan Inst. Chem. Eng.* **2017**, *74*, 25–48. [[CrossRef](#)]
43. Poudel, M.B.; Awasthi, G.P.; Kim, H.J. Novel insight into the adsorption of Cr(VI) and Pb(II) ions by MOF derived Co-Al layered double hydroxide @hematite nanorods on 3D porous carbon nanofiber network. *Chem. Eng. J.* **2021**, *417*, 129312. [[CrossRef](#)]
44. Hughes, I.D.; Dane, M.; Ernst, A.; Hergert, W.; Luders, M.; Poulter, J.; Staunton, J.B.; Svane, A.; Szotek, Z.; Temmerman, W.M. Lanthanide contraction and magnetism in the heavy rare earth elements. *Nature* **2007**, *446*, 650–653. [[CrossRef](#)] [[PubMed](#)]
45. Kujawa, J.; Al Gharabli, S.; Szymczyk, A.; Terzyk, A.P.; Boncel, S.; Knozowska, K.; Li, G.; Kujawski, W. On membrane-based approaches for rare earths separation and extraction—Recent developments. *Coord. Chem. Rev.* **2023**, *493*, 215340. [[CrossRef](#)]
46. Molina, L.; Gaete, J.; Alfaro, I.; Ide, V.; Valenzuela, F.; Parada, J.; Basualto, C. Synthesis and characterization of magnetite nanoparticles functionalized with organophosphorus compounds and its application as an adsorbent for La (III), Nd (III) and Pr (III) ions from aqueous solutions. *J. Mol. Liq.* **2019**, *275*, 178–191. [[CrossRef](#)]
47. Javadian, H.; Ruiz, M.; Sastre, A.M. Response surface methodology based on central composite design for simultaneous adsorption of rare earth elements using nanoporous calcium alginate/carboxymethyl chitosan microbiocomposite powder containing Ni_{0.2}Zn_{0.2}Fe_{2.6}O₄ magnetic nanoparticles: Batch and column studies. *Int. J. Biol. Macromol.* **2020**, *154*, 937–953. [[CrossRef](#)] [[PubMed](#)]
48. Han, L.; Peng, Y.; Ma, J.; Shi, Z.; Jia, Q. Construction of hypercrosslinked polymers with styrene-based copolymer precursor for adsorption of rare earth elements. *Sep. Purif. Technol.* **2022**, *285*, 120378. [[CrossRef](#)]
49. Zhu, J.; Chen, F.; Gan, M. Controllable biosynthesis of nanoscale schwertmannite and the application in heavy metal effective removal. *Appl. Surf. Sci.* **2020**, *529*, 147012. [[CrossRef](#)]
50. Zhou, F.; Xiao, Y.; Guo, M.; Wang, S.; Qiu, R.; Morel, J.L.; Simonnot, M.O.; Zhang, W.X.; Zhang, W.; Tang, Y.T. Insights into the Selective Transformation of Ceria Sulfation and Iron/Manganese Mineralization for Enhancing the Selective Recovery of Rare Earth Elements. *Environ. Sci. Technol.* **2023**, *57*, 3357–3368. [[CrossRef](#)]
51. Gunawardhana, B.P.N.; Gunathilake, C.A.; Dayananda, K.E.D.Y.T.; Dissanayake, D.M.S.N.; Mantilaka, M.M.M.G.P.G.; Kalpage, C.S.; Rathnayake, R.M.L.D.; Rajapakse, R.M.G.; Manchanda, A.S.; Etampawala, T.N.B.; et al. Synthesis of Hematite Nanodiscs from Natural Laterites and Investigating Their Adsorption Capability of Removing Ni²⁺ and Cd²⁺ Ions from Aqueous Solutions. *J. Compos. Sci.* **2020**, *4*, 57. [[CrossRef](#)]
52. Zhang, C.; Yu, Z.; Zeng, G.; Huang, B.; Dong, H.; Huang, J.; Yang, Z.; Wei, J.; Hu, L.; Zhang, Q. Phase transformation of crystalline iron oxides and their adsorption abilities for Pb and Cd. *Chem. Eng. J.* **2016**, *284*, 247–259. [[CrossRef](#)]

Disclaimer/Publisher's Note: The statements, opinions and data contained in all publications are solely those of the individual author(s) and contributor(s) and not of MDPI and/or the editor(s). MDPI and/or the editor(s) disclaim responsibility for any injury to people or property resulting from any ideas, methods, instructions or products referred to in the content.